

# A New Topology of Higher Order Power Filter for Single-Phase Grid-Tied Voltage-Source Inverters

Arash Anzalchi, *Student Member, IEEE*, Masood Moghaddami, *Student Member, IEEE*, Amir Moghaddasi, *Student Member, IEEE*, Arif I. Sarwat, *Senior Member, IEEE*, and Akshay K. Rathore, *Senior Member, IEEE*

**Abstract**—In order to reduce the influence of the grid harmonic currents and voltages, harmonic compensation is regularly implemented for a grid-tied inverter. In this study, a new topology of a higher order power filter for single-phase grid-tied voltage-source inverters, named  $L(LCL)_2$ , is presented. The subscript is added to the name to prevent confusion with the  $LLCL$  filter. In the proposed design, the inverter side inductance is divided into three parts, and the grid side inductor is removed. Also, an additional resonant branch at the double of the switching frequency is added to the traditional  $LLCL$  filter to attenuate high-frequency harmonics. The overall inductance of the recommended filter is smaller than the  $LLCL$  filter. A comparative study and discussions on the subject of the traditional  $LLCL$  filter and the proposed  $L(LCL)_2$  filter have been conducted and assessed through an experimental hardware implementation on a 700 W, 120 V/60 Hz single-phase grid-tied inverter. Furthermore, a straightforward engineering design benchmark is suggested to discover parameters of the  $L(LCL)_2$  filter. Moreover, stability analysis, loss analysis and an optimization of the  $L(LCL)_2$  filter parameters have been conducted in this study. The analysis shows that in comparison with the  $LLCL$  filter, the  $L(LCL)_2$  filter not only has lower voltage drop and less total inductor size, but also has improved performance in decreasing high-order current harmonics.

**Index Terms**—Grid-tied voltage-source inverter (VSI), harmonics,  $LCL$  filter,  $LLCL$  filter,  $L(LCL)_2$  filter, power quality, switching frequency.

## I. INTRODUCTION

As renewable energy systems, especially photovoltaics, are gaining more and more consideration, the grid-tied inverter has been extensively accepted. In order to limit unnecessary current harmonics, which are typically created by pulse width modulation (PWM), a low-pass power filter is regularly

Manuscript received December 8, 2015; revised March 9, 2016 and May 18, 2016; accepted June 7, 2016. Date of publication July 27, 2016; date of current version November 8, 2016. This work was supported in part by the National Science Foundation under Grant 1553494.

A. Anzalchi, M. Moghaddami, A. Moghaddasi, and A. I. Sarwat are with the Department of Electrical and Computer Engineering, Florida International University, Miami, FL 33174 USA (e-mail: aanza005@fiu.edu; mmogh003@fiu.edu; amogh004@fiu.edu; asarwat@fiu.edu).

A. K. Rathore is with the Department of Electrical and Computer Engineering, National University of Singapore, Singapore 119077 (e-mail: eleakr@nus.edu.sg).

Color versions of one or more of the figures in this paper are available online at <http://ieeexplore.ieee.org>.

Digital Object Identifier 10.1109/TIE.2016.2594222

placed between a voltage-source inverter (VSI) and the grid [1], [2].  $L$  filters are normally used, but they have the drawbacks of slow dynamic response and big inductor value [3], [4]. In comparison to a first-order  $L$  filter, an  $LCL$  filter can satisfy the standards for the grid interconnection with notably smaller size and cost, primarily for applications in several kilowatts [5]. Due to the growing cost of copper, various methods have been implemented to cut down the price of the power filter. A practical procedure is to increase the switching frequency of the inverter where the method, surely, depends on the device proficiency and cost.

Other measures, such as special topologies or controls, have been focused on by researchers [6]. With the intention of achieving a higher switching frequency and efficiency, a three-level neutral point clamped converter as a high-power renewable energy grid interface was presented in [7]. In [8] and [9], dual-mode time-sharing control methods for single- and three-phase inverters, correspondingly, were recommended to enlarge the modulation index and decrease the power filter size. However, these suggestions make the control methods or topologies more complicated, which leads to less reliability. Besides, it is very problematic for a dual-mode timesharing type inverter to reduce the harmonics or produce reactive power for the power grid. Saridakis *et al.* [10] present a new design technique, which employs SiC-type power devices for switching frequency optimization and improvement of the structure of the  $LCL$ -type output filter in transformerless PV inverters.

The total power loss of the  $LCL$  filter was used as the optimization factor in the designing of the filter parameters in [11]. The work in [11], explores the  $LCL$  filter design method from the perspective of efficiency and reduction in size and weight (and therefore cost). Nowadays, most power electronic designs are limited by thermal constraints. Power dissipation and surface area have a major influence on temperature change. The volume and size of the component are two measures that the surface area of the object is directly linked with. Moreover, when it comes to the industry, price is a vital aspect of selecting the power filter in a grid-tied inverter. Recently, for more reduction of the inductor size, the  $LLCL$ -filter has been proposed in [12]. Unlike the  $LCL$  filter, it can save on total cost and material since the grid-side inductance can be significantly reduced.

In [13], the topology of multiple shunt  $RLC$  trap filters has been analyzed, but the detailed design process was not given. Several optimized-filter designs, common-mode voltage

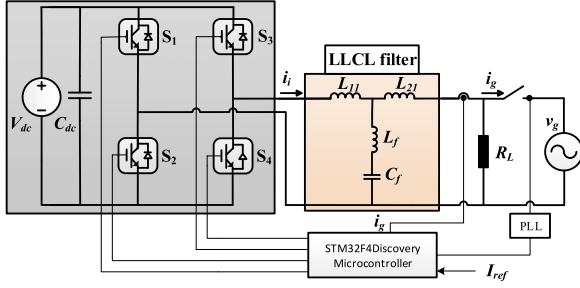


Fig. 1. Schematic diagram of the LLCL filter.

suppression methods, recommendations, and standards were also proposed in [14]–[16].

The objective of this paper is to propose a modified high-order filter design, named  $L(LCL)_2$  filter, based on the LLCL filter. The proposed filter can reduce the harmonics at the switching frequency and multiples of the switching frequency while saving the total inductance and thereby resulting in size reduction of the filter. The most important role of the grid-side inductor in the traditional LLCL filter is to decrease the harmonics around twice of the switching frequency. In the new topology, this inductor is removed, and the inverter-side inductor is split into three parts. Then, two resonant traps at the switching frequency and double of the switching frequency are inserted in between the inverter-side inductor. The proposed filter is able to attenuate the current ripple components better than the LCL and the LLCL filters.

The outline of the rest of the paper is as follows: First, the principle of an LLCL filter is presented. Then, a new engineering design procedure and parameter optimization of the high-order power filter is proposed and analyzed. Additionally, the closed-loop stability is assessed. Finally, experimental results on a 700 W, 120 V/60 Hz single-phase grid-tied inverter prototype with LLCL and  $L(LCL)_2$  filters are carried out and compared to confirm the correctness of theoretical analysis.

## II. PRINCIPLES OF THE LLCL-FILTERS

The circuit configuration of an LLCL-filter-based single-phase grid-tied VSI is illustrated in Fig. 1. The output voltage and current of the inverter are represented as  $v_i$  and  $i_i$ , and the grid voltage and current are represented as  $v_g$  and  $i_g$ . The switching frequency is shown as  $f_s$  (in hertz) or  $\omega_s$  (in radians per second). To simplify the analysis, the power grid is assumed to be a perfect voltage source with zero impedance, to supply a continuous voltage at the frequency of 60 Hz.

The instantaneous output voltage  $v_i(t)$  of the single-phase full-bridge VSI can be calculated as (1) while it is utilized under the situation of sine-triangle, unipolar, and asymmetrical regular sampled PWM [17]

$$v_i(t) = mV_{dc} \cos(\omega_0 t) + \sum_{k=1}^{\infty} \sum_{n=\pm 1}^{\pm \infty} \frac{2V_{dc} J_n(k\pi m)}{k\pi} \sin\left(\frac{n\pi}{2}\right) \cos(k\omega_s t + n\omega_0 t) \quad (1)$$

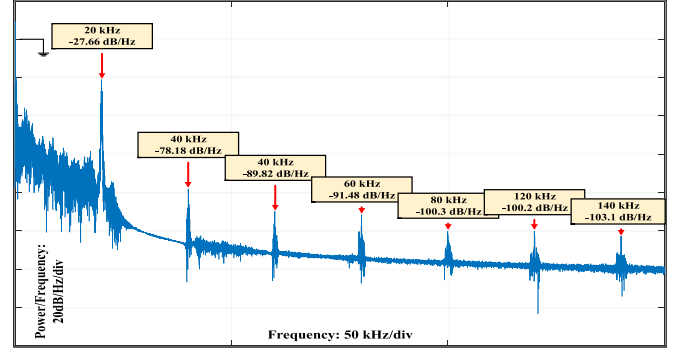


Fig. 2. Main harmonic current power density spectrum of inverter using unipolar modulation.

where  $m$  is the modulation index,  $V_{dc}$  is the dc-link voltage,  $\omega_0$  is the fundamental frequency, and  $J_n(x)$  is referred as the integrals of the Bessel function, which is known as  $J_n(x) = \int_0^\pi \cos(n\pi - x \sin t) dt$ , representing the sideband harmonic magnitude.

The inverter output impedance while  $\omega \neq \omega_0$  can be written as

$$Z_0(j\omega) = \frac{v_i(j\omega)}{i_i(j\omega)} \Big|_{v_g(j\omega)=0} = \frac{(L_{11}L_{21}C_f + (L_{11} + L_{21})L_f C_f)(j\omega)^3 + (L_{11} + L_{21})(j\omega)}{(L_{21} + L_f)C_f(j\omega)^2 + 1} \quad (2)$$

The grid-side current  $i_g$  is supposed as the ideal continuous current at the fundamental frequency (considering the harmonic current recommendation in IEEE 519-2014 and IEEE 1547.2-2008 [18], [19]). With that in mind, the branch circuit of inductor  $L_{21}$  can be seen as being opened by considering the effects of the inverter high-frequency harmonics.

The amplitudes of harmonics of inverter-side current  $i_i$  can be derived as

$$|I_H|_{|\omega \neq \omega_0} = \frac{|V_H(n, k)|}{|Z_0(j\omega)|} \quad (3)$$

where the amplitude output voltage harmonic  $V_H(n, k)$  is

$$V_H(n, k) = \left| \frac{2V_{dc} J_n(k\pi m)}{k\pi} \sin\left(\frac{n\pi}{2}\right) \right| \quad (4)$$

when  $k = 1, 2, \dots, \infty$  and  $n = \pm 1, \pm 2, \dots, \infty$ .

Fig. 2 illustrates the major harmonic power density spectrum of the current output of the inverter. The dc-link voltage  $V_{dc}$  is 210 V, inverter-side current ripple is 16.4%  $I_{ref}$  ( $I_{ref}$  is fundamental peak current), and the switching frequency  $f_s$  is 20 kHz. The modulation index  $m$  is assumed to be 0.9. It is clear that the harmonics around the switching frequency and then multiples of the switching frequency are the topmost harmonics of the inverter output current. Consequently, the paralleled trap  $L_f C_f$  is mainly limited by the harmonics around the switching frequency and the grid-side inductor  $L_{21}$  is limited by double the switching frequency [20].

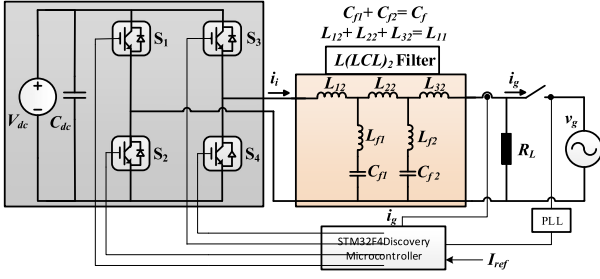


Fig. 3. Proposed  $L(LCL)_2$  system.

Assuming that the grid is an ideal sinusoidal voltage source, the transfer functions  $i_i(s)/v_i(s)$  can be calculated as

$$G_{u_i \rightarrow i_i}(s) = \left. \frac{i_i(s)}{v_i(s)} \right|_{v_g(s)=0} \quad (5)$$

$$= \frac{(L_{21} + L_f)C_f s^2 + 1}{(L_{11}L_{21}C_f + (L_{11} + L_{21})L_f C_f)s^3 + (L_{11} + L_{21})s}$$

and the transfer functions  $i_g(s)/v_i(s)$  of the  $LLCL$  filter can be expressed as

$$G_{u_i \rightarrow i_g}(s) = \left. \frac{i_g(s)}{v_i(s)} \right|_{v_g(s)=0} \quad (6)$$

$$= \frac{L_f C_f s^2 + 1}{(L_{11}L_{21}C_f + (L_{11} + L_{21})L_f C_f)s^3 + (L_{11} + L_{21})s}$$

### III. PROPOSED $L(LCL)_2$ FILTER

In this paper, a new topology of the  $LLCL$  filter structure is proposed, as also illustrated in Fig. 3, where the inverter-side inductance of the  $LLCL$  filter is separated into three sections in order to allow inserting resonant traps in between them. Also, the resonant capacitor of the traditional  $LLCL$  filter is divided into two capacitors to produce a new resonant branch at double the switching frequency. Consequently, the grid-side inductance of the  $LLCL$  filter ( $L_{21}$ ) can be removed. As a result, since the total amount of the capacitor does not change, the capacitive reactive power at rated load will remain constant. Compared to the conventional  $LLCL$  filter-based system, the additional trap inserted between the grid-side inductance does not add to the control difficulties of the system. Actually, it reduces the size of the electromagnetic part of the system, which leads to a more efficient low-pass filter. Considering  $A(s)$  and  $M(s)$  definitions as

$$A(s) = \frac{Z_2(s)Z_{f2}(s)}{Z_2(s) + Z_{f2}(s)}, M(s) = \frac{Z_2(s)}{Z_{f2}(s)} + 1 \quad (7)$$

where  $Z_1(s) = sL_{12}$ ,  $Z_2(s) = sL_{22} = sL_{32}$ ,  $Z_{f1}(s) = sL_{f1} + 1/sC_{f1}$  and  $Z_{f2}(s) = sL_{f2} + 1/sC_{f2}$ . The transfer functions  $i_1(s)/v_i(s)$  and the transfer functions  $i_g(s)/v_i(s)$  of the

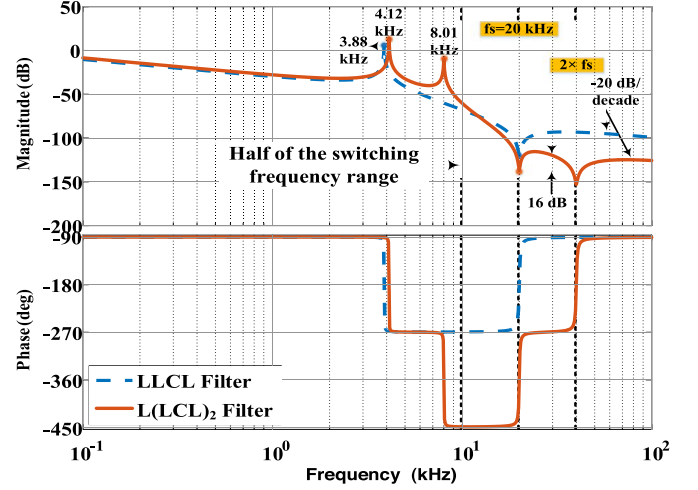


Fig. 4. Bode plots of transfer functions  $i_g(s)/v_i(s)$ .

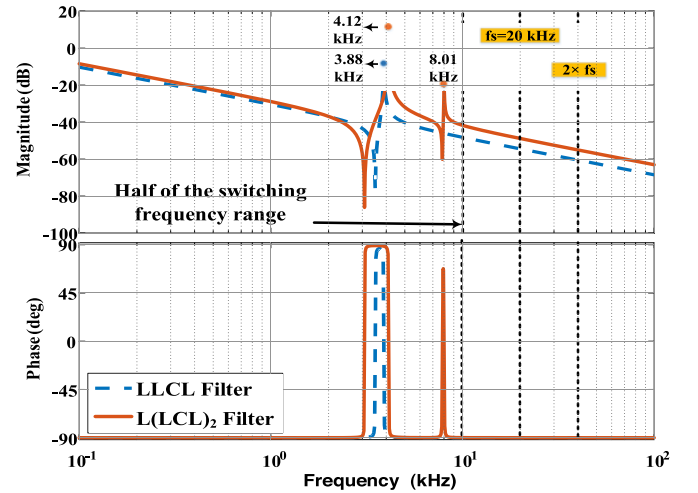


Fig. 5. Bode plots of transfer functions  $i_i(s)/v_i(s)$ .

$L(LCL)_2$  filter can be, respectively, calculated as

$$G_{u_i \rightarrow i_i}(s) = \left. \frac{i_i(s)}{v_i(s)} \right|_{v_g(s)=0} \quad (8)$$

$$= \frac{A + Z_2 + Z_{f1}}{(A + Z_2 + Z_1)Z_{f1} + (A + Z_2)Z_1}$$

$$G_{u_i \rightarrow i_g}(s) = \left. \frac{i_g(s)}{v_i(s)} \right|_{v_g(s)=0} \quad (9)$$

$$= \frac{Z_{f1}}{Z_2(M + Z_{f1}(M + Z_2) + 1) + MZ_1Z_{f1}}$$

Fig. 4 shows bode plots of the transfer function  $i_g(s)/v_i(s)$  of both the  $L(LCL)_2$  filter and the  $LLCL$  filter, while all the other parameters are the same, except inductances of the traps. Also,  $L_{11}$  in the  $LLCL$  filter is divided into three parts and  $C_f$  is divided into two capacitors. Fig. 5 presents bode plots of the transfer function  $i_i(s)/v_i(s)$  with aforementioned parameters. The

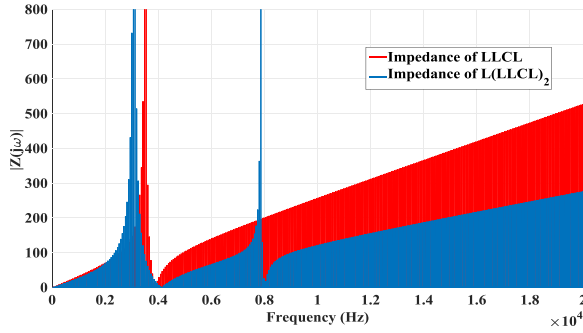


Fig. 6. Size of the impedance of the  $LLCL$  and the  $L(LLCL)_2$  filters for different frequencies.

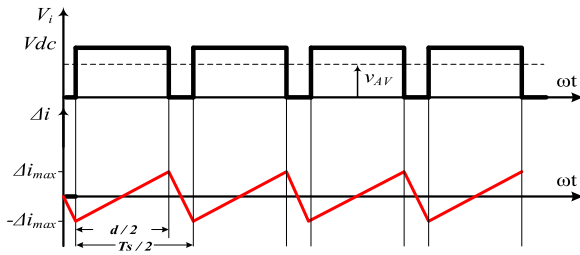


Fig. 7. Voltage and the current output waveform of typical single-phase full-bridge inverters.

figures help in verifying that all the requirements are satisfied with the design. It is clear that within half of the switching frequency range, the  $L(LLCL)_2$  filter has a nearly identical frequency response pattern of an  $LLCL$  filter, and both resonant frequencies match the resonant frequency criteria of the low-pass filters for having a stable system. That is to say, compared to an ordinary  $LLCL$  filter, the additional  $C_{f2}L_{f2}$  branch of the  $LLCL$  filter does not bring any further control worries. Fig. 6 shows the size of the total impedance of the  $L(LLCL)_2$  filter when frequency varies from 0 to 20 kHz. It can be seen that the impedance of the proposed filter is lower than the  $LLCL$  filter, except around resonant frequencies of the filters.

### A. Analysis of Ripple Current

The time average value of the output voltage of the inverter,  $v_{AV}$ , can be assumed constant during the switching period  $T_s$ , if the switching frequency  $f_s$  is greater than the grid frequency  $f_0$ .

Hence, the current of the filter inductor of the grid-tied single-phase full-bridge inverters has a symbolic curve for the duration of any period, as illustrated by the lower waveform in Fig. 7. In this situation,  $\Delta i_{pp}$ , the peak-to-peak value of the filter inductor current, which is generated by the unipolar PWM switching, can be calculated as [21]

$$\Delta i_{pp} = 2\Delta i_{max} = \frac{V_{dc} - v_{AV}}{L} \frac{d}{2} T_s \quad (10)$$

where  $L$  is the inverter-side inductor of any kind of filter (including  $LCL$ ,  $LLCL$ ,  $L(LLCL)_2$ , etc.). Moreover, grid voltage  $v_g$  is supposed to be a clean sinusoidal waveform. To make the

analysis simpler, the fundamental component of the grid current in Fig. 3 is pretended to be zero. Consequently, the fundamental component of the voltage appears on the filter inductor is similarly zero as

$$v_L = v_i - v_g = 0. \quad (11)$$

Therefore, when  $0 < \omega t < \pi$ , (12) and (13) can be calculated as

$$v_{AV}(\omega t) = d(\omega t)V_{dc}, v_g(\omega t) = m \cdot V_{dc} \sin(\omega t) \quad (12)$$

$$d(\omega t) = m \cdot \sin(\omega t) \quad (13)$$

and during  $0 < \omega t < \pi$ , the peak-to-peak value of the current of the filter inductor will be [22]

$$\Delta i_{pp}(\omega t) = \frac{V_{dc} T_s}{4L} (1 - m^2 \cdot \sin^2(\omega t)). \quad (14)$$

### B. Parameter Design of the $L(LLCL)_2$ Filter

Some limitations were introduced by [4], [12] to be considered when designing the  $LCL$  and  $LLCL$  filters, which could be used in the  $L(LLCL)_2$  filter.

- 1) The total capacitive reactive power at rated load should be less than 5% of the nominal power and capacitors are limited by this constraint.
- 2) The total inductance is limited by the voltage drop for the duration of operation (less than 10%). If not, the dc-link voltage will be required to be higher to guarantee controllability of current, which will cause greater losses in switching devices.
- 3) The range of the resonant frequency ought to be bigger than ten times the line frequency or one-sixth of the switching frequency (whichever is higher) and one-half of the switching frequency, with the intention of keeping away from control and stability problems, which possibly were caused by resonance in the upper and the lower parts of the harmonic spectrum.
- 4) The inverter-side inductor  $L_{12}$  is constrained by the maximum ripple current requirement (normally  $\leq 40\%$ ).
- 5) Considering IEEE 519-2014, the harmonics greater than the 35th should be less than 0.3% of the rated fundamental current, if the short-circuit current of the system is less than 20 times of the fundamental grid-side current.

Considering the mentioned constraints, the  $L(LLCL)_2$  filter can be designed by using the following steps:

- 1) With the intention of meeting a particular requirement for current ripple, the inductance can be designed from

$$\frac{V_{dc}}{4f_s(\alpha_1 I_{ref})} \geq L_{11} \geq \frac{V_{dc}}{4f_s(\alpha_2 I_{ref})} \quad (15)$$

where  $I_{ref}$  is the rated reference peak current,  $\alpha_1$  and  $\alpha_2$  are the inverter-side current ripple ratio, which generally have the value of 15% and 40%, respectively. This inductance is the amount of total inductance of the filter ( $L_{11} = L_{12} + L_{22} + L_{32}$ ), while  $L_{12} = K \times L_{11}$  ( $33\% < K < 60\%$ ) and  $L_{22} = L_{32} = (L_{11} - L_{12})/2$ .

- 2) By selecting the absorption of reactive power, while the system is operating in rated conditions, the capacitor

value can be determined

$$C_f(\text{Total}) = xC_b \quad (16)$$

where  $x$  is the absorbed reactive power percentage at full-load conditions ( $x < 1$ ). The total capacitor number is limited by

$$C_{\max} = \frac{5\%P_{\text{rated}}}{V_g^2\omega_0}. \quad (17)$$

Then the capacitor of each branch is almost half of the total capacitor in the  $LLCL$  filter.

- 3) The resonant frequency of the  $L_{f1}C_{f1}$  and the  $L_{f2}C_{f2}$  circuits are at the switching frequency and the double of the switching frequency, respectively. Thus,  $L_{f1}$  and  $L_{f2}$  can be calculated by

$$\frac{1}{\sqrt{L_{f1}C_{f1}}} = \omega_{s1}, \quad \frac{1}{\sqrt{L_{f2}C_{f2}}} = \omega_{s2} \quad (18)$$

where  $\omega_{s1}$  is the switching frequency and  $\omega_{s2}$  is twice the switching frequency.

- 4) In  $LLCL$  filters, grid-side inductance  $L_{21}$  is mostly used to reduce each harmonic around twice the switching frequency down to 0.3%. For an  $L(LCL)_2$  filter, due to the additional  $L_{f2}C_{f2}$  branch, the current harmonics near the double of the switching frequency fulfill the IEEE 519-2014 standard with far more ease. Therefore,  $L_{21}$  is replaced by a portion of  $L_{11}$ .
- 5) The resonant frequency can be calculated by setting the dominator of (9) to zero, after replacing “ $s$ ” with “ $j\omega$ .” If it does not satisfy the requirement 3, absorbed reactive power can be changed, then return to step 2. Otherwise, the tolerable current ripple can be adjusted again, then return to step 1.
- 6) The quality factor of each resonant circuit should be  $10 \leq Q \leq 50$ , that can be calculated as

$$Q = \frac{1}{R_f} \sqrt{\frac{L_f}{C_f}} \quad (19)$$

where  $R_f$  is the gapped equivalent resistance of the inductors in the resonant branches ( $L_{f1}$  and  $L_{f2}$ ).

The most important limitations, such as the voltage drop across the inductor, the capacitive reactive power, and the amplitude of the harmonic currents, should be considered, while the design procedure is iterative with the  $L(LCL)_2$  parameter values adjusted. The algorithm for designing the  $L(LCL)_2$  filter is shown in Fig. 8.

### C. Design Example

Once designing a high-order filter for power inverters, the base values of the total impedance, inductance, and capacitance should be defined as

$$Z_b = \frac{v_g}{P_{\text{rated}}}, L_b = \frac{Z_b}{\omega_b}, C_b = \frac{1}{\omega_b Z_b} \quad (20)$$

where  $\omega_b$  is the grid frequency and  $P_{\text{rated}}$  is the rated active power of the inverter. Considering the constraints addressed in

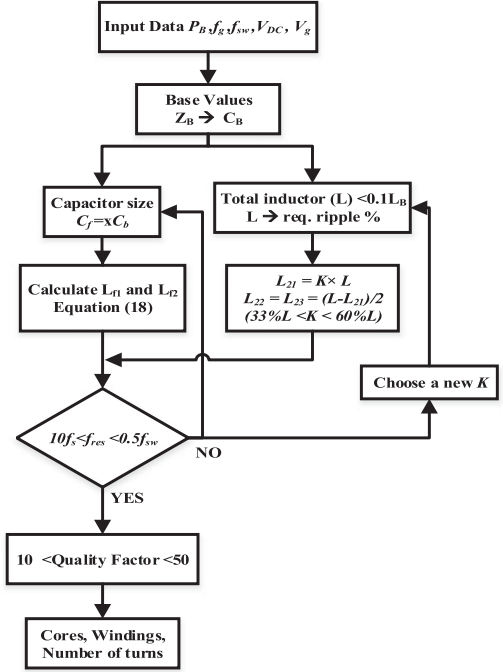


Fig. 8. Flowchart of the parameter design procedure of the  $L(LCL)_2$  filter.

Section II-A, and under the condition of that  $f_s = 20$  kHz,  $V_{dc} = 210$  V,  $P_{\text{rated}} = 700$  W, grid phase to ground voltage is 120 V/60 Hz. Then, the attenuation of the current harmonics focused on the design processes of the  $L(LCL)_2$  filter can be derived as follows:

- 1) By assuming the 7.7% impedance for the inverter-side inductor,  $L_{11}$  is selected to be 4.2 mH. For an  $LLCL$  filter,  $L_{21}$  mostly designed on the objective to decrease each harmonic around the double of the switching frequency down to 0.3%, but for the  $L(LCL)_2$  filter, owing to the  $L_{f2}C_{f2}$  resonate circuit, the twice of the switching frequency harmonics are approximately eliminated. Therefore, the calculated inductance for inverter-side inductance of the traditional  $LLCL$  filter is split into three smaller inductances. The first part has a value of  $L_{12} = 2.2$  mH (about 53% of calculated inverter-side inductance of the conventional  $LLCL$  filter), then  $L_{22} = 1$  mH and  $L_{32} = 1$  mH. The inverter-side inductor  $L_{12}$  should fulfill the requirements of (15). In this case, the value of inverter-side current ripple is 16.40%, which is in the range between 10% and 40%.
- 2) To achieve the limitation of the maximum absorbed reactive power at rated conditions, the total capacitance ( $C_{f1} + C_{f2}$ )  $\leq 0.05C_b$ . Hence, the capacitor value is designed to be  $C_{f1} + C_{f2} = 2 \mu\text{F}$  in order to limit the reactive power to 1.55%. This value can be increased to the limit of 5%, if some of the constraints cannot be met.
- 3) The grid-side inductor of  $L_{21}$  is removed in the  $L(LCL)_2$  filter, but  $L_{22}$  and  $L_{23}$  are two sections of the split inductor and both of them have the value of 1 (mH).

- 4) The consequent resonance frequency is 3.88 kHz for the  $LLCL$ , and the  $L(LCL)_2$  filter has two resonant frequencies at 4.12 kHz and 8.01 kHz. Both resonant frequencies of the  $L(LCL)_2$  are between one half of the switching frequency and one-sixth of the switching frequency.
- 5) The quality factor of resonant branches is chosen to be 50, and the equivalent resistor value of  $R_{f1}$  is  $0.16 \Omega$  and  $R_{f2}$  is  $0.08 \Omega$ .

#### D. Optimization of the $L(LCL)_2$ Parameters

Frequent trial and error in the design procedure increases the need to conduct an optimization of  $L(LCL)_2$  filter on MATLAB software. Due to the connection between the filter parameters and the device performance indexes, the optimization is based on the total harmonic distortion (THD). Although, some useful trial-and-error solutions with computer programs can be achieved, for instance, in [23]. Changes of several performance indexes could be caused by the variation of one of the filter parameters. For building an accurate THD model, the harmonics caused by power switches and the control loop should be taken into consideration. The current harmonics provided by closed-loop transfer functions of the  $L(LCL)_2$  filter can be expressed as follows [24] where  $v_i(t)$  is calculated by (1) and the open-loop transfer function of the  $L(LCL)_2$  filter  $G(s)$  can be calculated by (9). According to [24], the goal of optimization is to find the minimum values of  $L_{12}$ ,  $L_{22}$ , and  $L_{32}$  on the basis of the allowable THD. The objective function for genetic algorithm (GA) optimization can be expressed as

$$\min f(x) = \left(2 + \frac{1}{r}\right) L_{22} (x = [L_{22}, r, C_{f1}, C_{f2}]) \quad (21)$$

when  $L_{22} = L_{23}$  and  $r = L_{22}/L_{12}$ . To leave a certain margin, the restrictive value of THD can be chosen as 3% (instead of 5%). GA is an effective method to find the optimal solution. The constraint can be expressed as  $L_{12}$ ,  $L_{22}$ , and  $L_{32}$  on the premise of the allowable THD. The objective function for GA optimization can be expressed as

$$\text{THD}(x) = 3\%. \quad (22)$$

The parameter variety can be obtained from Section III-B. On this basis, the allowed range of  $L_{22}$ ,  $r$ ,  $C_{f1}$  and  $C_{f2}$  are  $0.311 \text{ mH} \leq L_{22} = L_{32} \leq 1.505 \text{ mH}$ ,  $0.07 \leq r \leq 1.19$ ,  $0.5 \mu\text{F} \leq C_{f1}, C_{f2} \leq 3 \mu\text{F}$ . With the initial values of [0.908 mH, 0.63, 1.75  $\mu\text{F}$ , 1.75  $\mu\text{F}$ ], the optimized result is [0.918 mH, 0.42, 0.935  $\mu\text{F}$ , 0.941  $\mu\text{F}$ ]. In the real world, capacitors have a series of fixed values. The one which is the closest to 0.935  $\mu\text{F}$  and 0.941  $\mu\text{F}$  is 1  $\mu\text{F}$ . Therefore, the values of the  $C_{f1}$  and the  $C_{f2}$  are chosen as 1  $\mu\text{F}$ . When the fixed value of  $C_{f1}$  and  $C_{f2}$  are considered, the parameters of the  $L(LCL)_2$  filter are chosen as [1.02 mH, 0.43, 1  $\mu\text{F}$ , 1  $\mu\text{F}$ ]. Comparing with the step-by-step method, these values have 2%, 2.3%, 0%, and 0% error, respectively. These errors are within an acceptable range.

#### E. Closed-Loop Stability Analysis

Many techniques are used for the analysis of the stability of a system. A popular technique is analysis of the eigenvalues

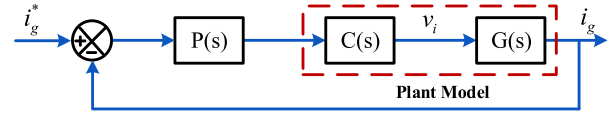


Fig. 9. Block diagram of the current control system.

TABLE I  
DESIGNED PARAMETERS FOR EXPERIMENTAL SETUP

Elements	Parameters	Values
Inverter	DC-link voltage ( $V_{dc}$ )	210 V
	Switching frequency ( $f_s$ )	20 kHz
	Rated power ( $P_{rate}$ )	700 W
AC grid	Grid phase voltage ( $v_g$ )	120 V
	Grid frequency ( $f_0$ )	60 Hz
$L(LCL)_2$ filter	Inverter-side inductor ( $L_{12}$ )	2.2 mH
	Grid side inductors ( $L_{22} = L_{32}$ )	1 mH
	Resonant circuit inductor ( $L_{f1}$ )	63.3 $\mu\text{H}$
	Resonant circuit inductor ( $L_{f2}$ )	15.83 $\mu\text{H}$
	Resonant circuit capacitors ( $C_{f1} = C_{f2}$ )	1 $\mu\text{F}$
	Equivalent resistance of the inductor ( $R_{f1}$ )	0.16 $\Omega$
$LLCL$ filter	Equivalent resistance of the inductor ( $R_{f2}$ )	0.08 $\Omega$
	Converter side inductor ( $L_{11}$ )	4.2 mH
	Grid side inductor ( $L_{21}$ )	1.2 mH
	Resonant circuit inductor ( $L_f$ )	31.67 $\mu\text{H}$
	Resonant circuit capacitor ( $C_f$ )	2 $\mu\text{F}$
	Equivalent resistance of the inductor ( $R_f$ )	0.11 $\Omega$

to study the system stability [25], [26], which is explained in this section. Fig. 9 shows the typical block diagram of a current controller, where  $P(s)$ ,  $C(s)$ , and  $G(s)$  are the model of the controller, inverter, and the proposed filter, respectively. A conventional PI controller is adopted as  $P(s)$  in order to achieve the specified dynamics, i.e.,

$$P(s) = \frac{(k_p s + k_I)}{s} \quad (23)$$

where  $k_p = 1$  is the proportional gain and  $k_I = 100$  is integral gain. These values are designed and tuned by the trial-and-error method. The system time delays due to discrete operation and phasor PWM blocks are neglected, i.e.,  $C(s) = 1$  and  $G(s)$  is calculated by (9), thus, the closed-loop transfer function of the current control system can be written as

$$H(s) = \frac{i_g(s)}{i_g^*(s)} = \frac{P(s)G(s)}{1 + P(s)G(s)}. \quad (24)$$

The eigenvalues of (24) determine the dynamics of the closed-loop system. Herein, the stability of the proposed system, with respect to the variation in system matrix parameters, is studied. This study is based on a 700 w laboratory prototype, in which parameters are summarized in Table I. The eigenvalues of the system at this operating point are  $\lambda_{1,2} = -119.04 \pm j98.16$ ,  $\lambda_{2,3} = -288.88 \pm j25872.9$ , and  $\lambda_{4,5} = -1401.15 \pm j50313.5$ . The real parts of all six eigenvalues are negative, which signifies the linearized system's stability. However, the stability of the overall system cannot be guaranteed for all values of the filter parameters. Thus, for stability analysis, the eigenvalues of the system are plotted versus the variation of one parameter at a time, while the other nominal parameters remain constant.

It is worth mentioning that the range of the oscillation of all the parameters corresponds to the step-by-step design procedure in Section III. Furthermore, in transfer function (24), the system eigenvalues remain almost constant with  $\pm 20\%$  variations of the  $L_{f1}$  and the  $L_{f2}$ . In fact, the variation of the  $L_{f1}$  and  $L_{f2}$  does not affect the stability of the proposed system.

The impacts of  $L_{12}$  and  $L_{32}$  on the eigenvalues of the system are shown in Fig. 10(a) and (b), respectively, when  $L_{12}$  varies from 1.39 to 2.52 mH and  $L_{21}$  varies from 0.84 to 1.485 mH. Also,  $L_{22}$  is equal to  $L_{32}$ , so their variations are depicted together in Fig. 10(b).

It can be observed that the increase of the inverter-side and the grid-side inductances displaces all complex eigenvalues toward the vertical axis of the  $s$ -plan. Thus, it is predictable that the whole system's response becomes longer and less oscillatory as  $L_{12}$  and  $L_{32}$  increase.

The variation of system eigenvalues by varying the  $C_{f1}$  and  $C_{f2}$  from 0.5 to 3  $\mu\text{F}$  are shown in Fig. 10(c) and (d). As it can be seen, the impact of the  $C_{f1}$  and  $C_{f2}$  on the eigenvalues  $\lambda_1$  and  $\lambda_2$  are almost negligible. However, Fig. 10(c) shows that the complex eigenvalues  $\lambda_3$ ,  $\lambda_4$ ,  $\lambda_5$ , and  $\lambda_6$  move toward the real axis, which can reduce the system's natural frequencies and increases the damping factor of the system. Fig. 10(d) obviously demonstrates that all eigenvalues stay on the left half of the  $s$ -plane for the whole effective range, which presents the stability of the proposed system over the given range.

Fig. 10(e) and (f) illustrates the eigenvalues of the proposed system as  $R_{f1}$  and  $R_{f2}$  vary from 0.08 to 0.39  $\Omega$  and 0.16 to 0.8  $\Omega$ , respectively. As can be seen, increasing the resistances of the filter results in moving the real part of eigenvalues  $\lambda_3$ ,  $\lambda_4$ ,  $\lambda_5$ , and  $\lambda_6$  toward the left, and therefore, a faster response and less oscillatory. However, increase of the resistance increases the power losses of the system, which is usually undesirable.

#### IV. EXPERIMENTAL RESULTS

With the purpose of confirming the effectiveness of the suggested  $L(LCL)_2$  filter on attenuating the current harmonics, a 700 W prototype of the single-phase full-bridge grid-tied inverter with the "STM32F4" microcontroller is constructed. The experimental parameters of the proposed filter are listed in Table I.

The experiments are investigated and evaluated under the given conditions of  $f_s = 20$  kHz,  $V_{dc} = 210$  V,  $v_g = 120$  V/60 Hz,  $P_{rated} = 700$  W, and SPWM strategy is used in the inverter. Also, a boost converter is used to step-up the voltage of the renewable power supply (86 V) to 210 V and keep the dc-link voltage at this level. The switching frequency of the boost converter is 20 kHz.

Case I is the traditional  $LLCL$  filter strategy and Case II is the  $L(LCL)_2$  filter strategy with an extra trap at 40 kHz. Figs. 11–15 show important system variables, which were captured with a LeCroy WaveRunner 64Xi oscilloscope.

Figs. 11 and 12 show the grid-side current–voltage waveforms and the power density spectrum of the grid-side currents for cases I and II, respectively. In Figs. 11(b) and 12(b), it is illustrated that the power density of the current harmonics around

20 kHz is reduced by the factor of 3.99 dB/Hz from case I to case II, but the power density around 40 kHz increased from  $-103.10$  B/Hz (case I) to  $-102.56$  dB/Hz (case II). Hence, the most dominant current harmonics are diminished even more than the previous design. However, a small increase occurred at double the switching frequency, but as the power density is too small ( $-103.10$  dB/Hz), it can be neglected. Therefore, the performance of the filter is improved.

The currents flowing through the resonant branches for Case I and Case II are shown in Figs. 13–15, while the grid current is 5.8 A and the voltage is 120 V. The magnitude of the currents in  $L_{f1}C_{f1}$  and  $L_{f2}C_{f2}$  traps are almost half of the  $L_fC_f$  trap and that is because the impedance of both traps of the  $L(LCL)_2$  filter is 2.652 k $\Omega$  (at 60 Hz), but the  $LLCL$  filter has an impedance of 1.326 k $\Omega$ . Also, it can be seen that the power density of current harmonics at the switching frequency and multiples of the switching frequency are almost the same in the  $L_fC_f$  branch of the  $LLCL$  and the  $L_{f1}C_{f1}$  branch of the  $L(LCL)_2$  filter. In addition to that, more attenuation occurs at the  $L_{f2}C_{f2}$ . The measured THD% of  $i_g$  in Cases I and II are 2.06% and 1.90%, respectively, and THD of  $v_g$  in Cases I and II are 1.41% and 1.36%, respectively, which shows the effectiveness of the designed filter in improving the THD of the grid current and voltage.

Fig. 16 shows the bode plots of the  $i_g(s)/v_i(s)$  transfer function for different values of the series and the resonant branch inductances. Obviously, when the values of  $L_{12}$ ,  $L_{22}$ , and  $L_{32}$  are in the range of parameter values generated by the proposed procedure, the resonant frequency variation meets the design criteria. Therefore, the system is still able to maintain stability. Furthermore, to guarantee that all current harmonic ( $\geq 35$ th) is less than 0.3% of the fundamental current, while it is assumed that the parameter variation of inductances of resonant branches are in a range of  $\pm 20\%$ , it is essential to investigate the ripple current harmonics both at  $f_s$  and at  $2f_s$  while these inductors change  $\pm 20\%$ . The harmonics of current around the switching frequency with  $L_{f1} \pm 20\%$  is 0.21% and the current harmonics around double the switching frequency with  $L_{f2} \pm 20\%$  is 0.017%.

The image of the laboratory setup of  $L(LCL)_2$ -filter-based inverter system is shown in Fig. 17. For building the inductances of  $LLCL$  and  $L(LCL)_2$  filters, ferrite cores with N87 material and epoxy coating are used.

#### V. ANALYSIS AND DISCUSSION

From the experimental results, the following can be seen:

- 1) In both cases, the dominating harmonic current meets the IEEE 519-2014 recommendation in the experiment. However, the current harmonic at 20 kHz has reduced, and the current harmonic at 40 kHz has the same value.
- 2) The value of the grid-side inductor is reduced in Case II, thus, the drop of the voltage during the operation is lower, and the dc-link voltage is the same in both cases.
- 3) The total value of the inductors of the  $L(LCL)_2$  filter is reduced by a factor of 22.22%, in comparison to that of the  $LLCL$  filter.

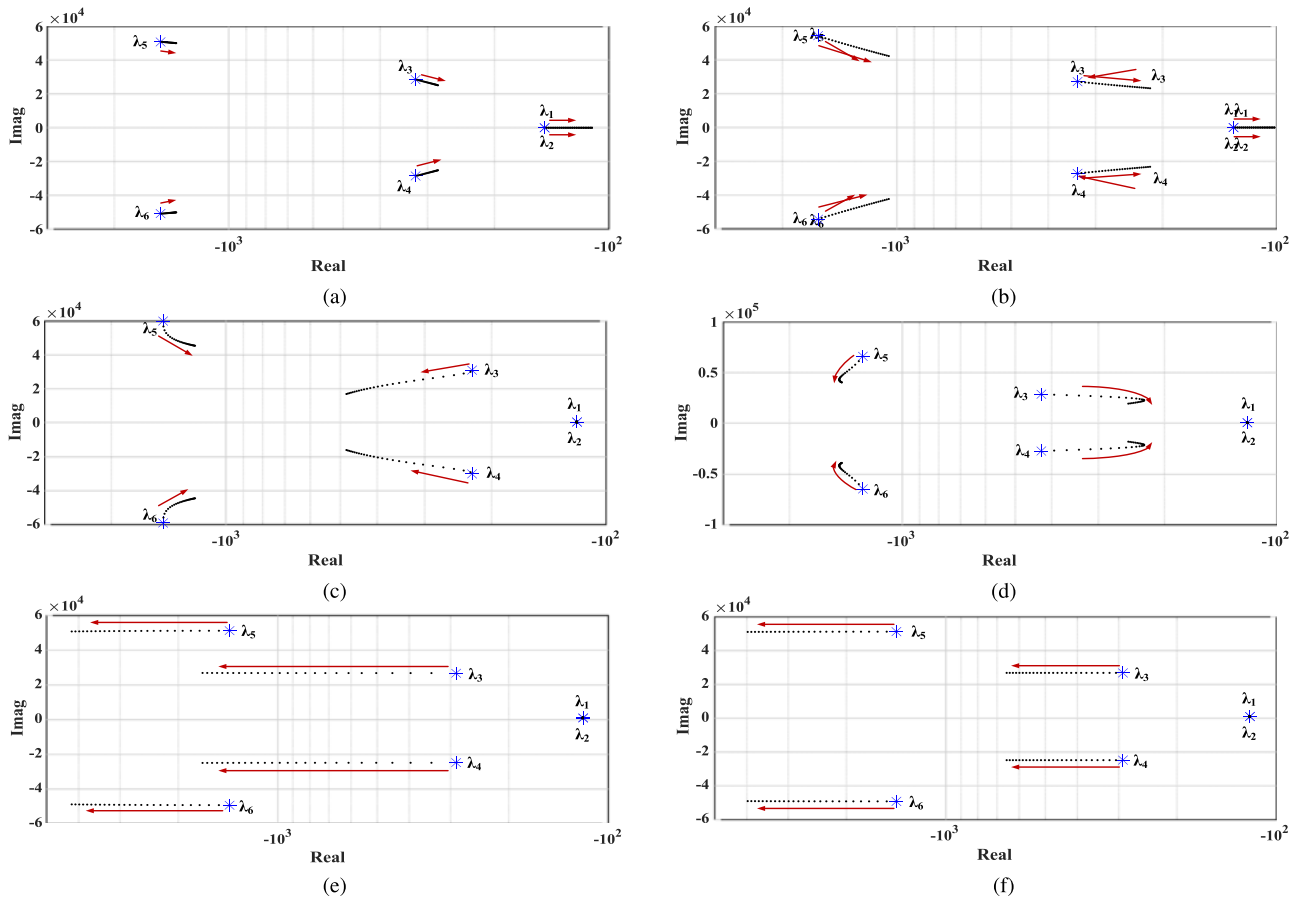


Fig. 10. Root locus of the closed-loop transfer function of the system ( $H_s$ ) as (a)  $L_{12}$  varies from 1.39 to 2.52 mH (b)  $L_{22}$  and  $L_{32}$  vary from 0.84 to 1.485 mH (c)  $C_{f1}$  varies from 0.5 to 3  $\mu\text{F}$  (d)  $C_{f2}$  varies from 0.5 to 3  $\mu\text{F}$  (e)  $R_{f1}$  varies from 0.08 to 0.39  $\Omega$ . (f)  $R_{f2}$  varies from 0.16 to 0.8  $\Omega$ .

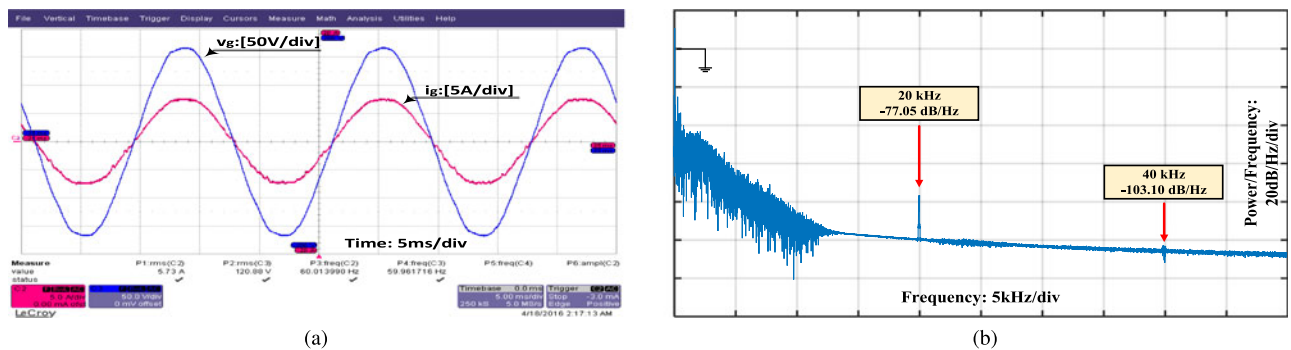


Fig. 11. Experimental waveforms with LLCL filter. (a) Grid voltage and grid-side current waveforms. (b) Power density spectrum of grid-side current.

- 4) The reactive power in the newly designed filter is the same as the traditional LLCL filter  $C_{f1} + C_{f2} = C_f$ .
- 5) Generally, the experimental results are in acceptable agreement with the theoretical study, particularly regarding the attenuation of the harmonic current around the switching frequency and double the switching frequency.

#### A. Power Loss Analysis of the $L(LCL)_2$ Filter Components

1) **High-Frequency Damping Loss:** Ignoring the grid voltage harmonics and the dead-time effect, the most dominating high-order current harmonics contain the switching frequency and the double of the switching frequency. The damping loss in

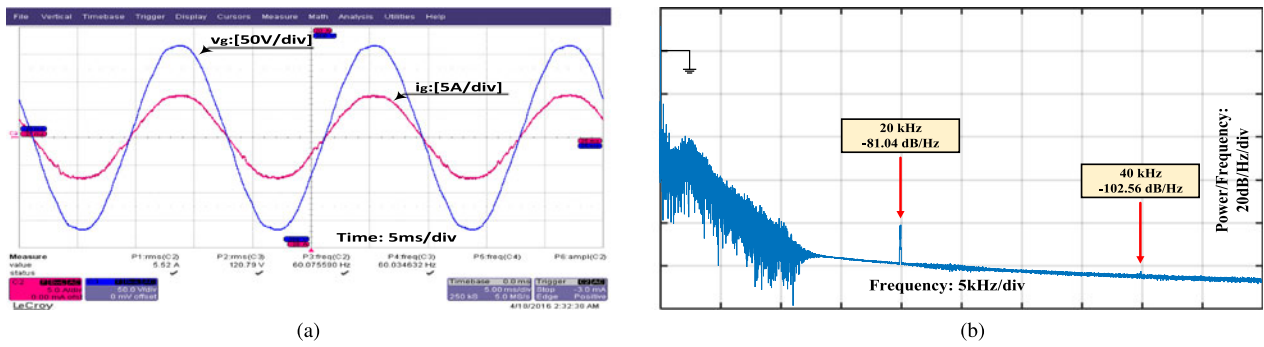


Fig. 12. Experimental waveforms with  $L(LCL)_2$  filter. (a) Grid voltage and grid-side current waveforms. (b) Power density spectrum of grid-side current.

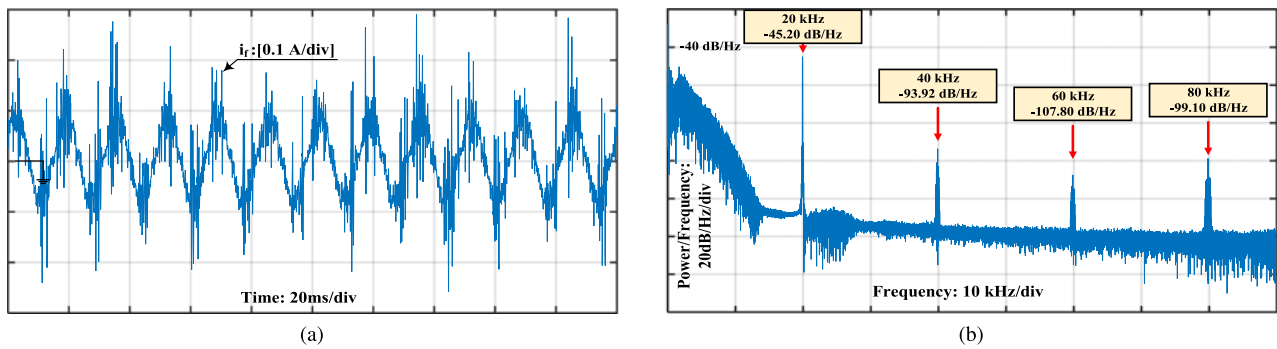


Fig. 13. (a)  $L_f-C_f$  current of  $LLCL$  filter. (b) Power spectral density of  $L_f-C_f$  current in  $LLCL$  filter.

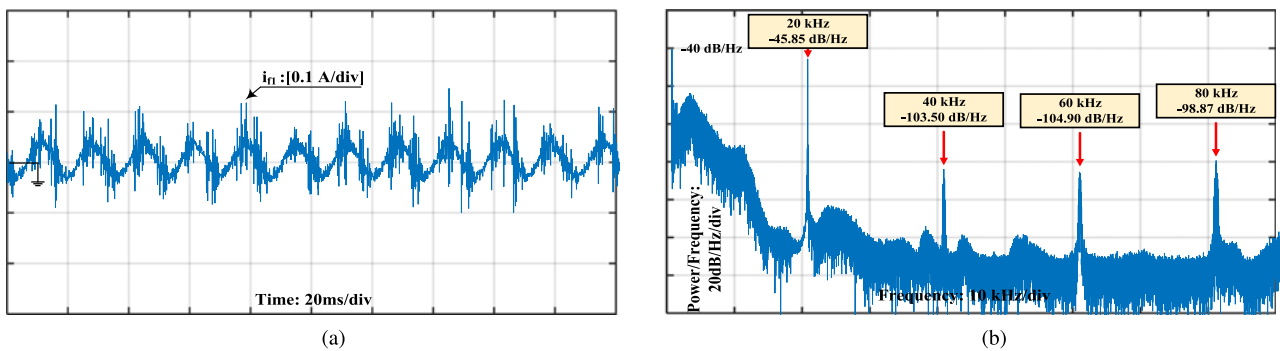


Fig. 14. (a) Current of switching frequency trap  $L_{f1}-C_{f1}$  of  $L(LCL)_2$  filter. (b) Power spectral density of  $L_{f1}-C_{f1}$  current in  $L(LCL)_2$  filter.

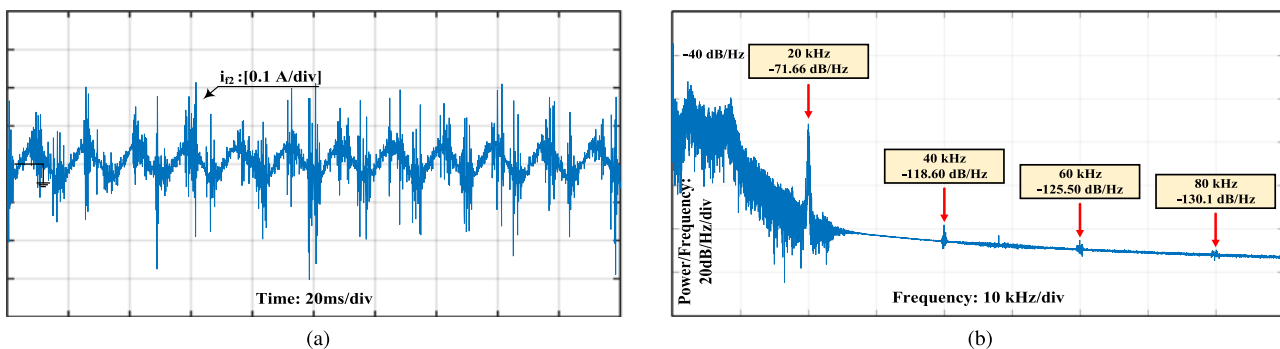


Fig. 15. (a) Current of double of switching frequency trap  $L_{f2}-C_{f2}$  of  $L(LCL)_2$  filter. (b) Power spectral density of  $L_{f2}-C_{f2}$  current in  $L(LCL)_2$  filter.

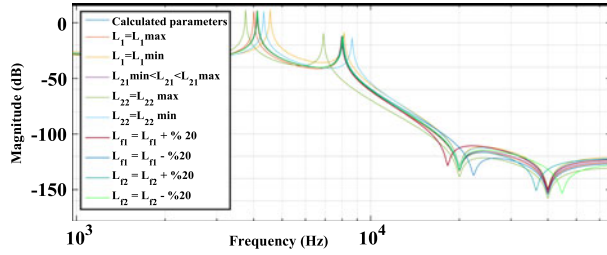


Fig. 16. Bode plots of transfer function  $i_g(s)/v_i(s)$  under different filter inductances.

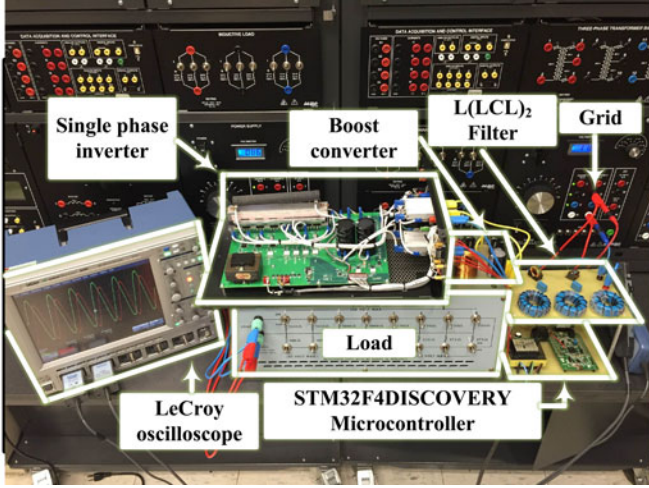


Fig. 17. Experimental setup.

the high frequency can be obtained as follows [27]:

$$P_d(\text{ripple}) = \frac{1}{2} |I_{AM}(n, k_1)|^2 \times R_{f1} + |I_{AM}(n, k_2)|^2 \times R_{f2} \quad (25)$$

where  $n = \pm 1, \pm 3, \pm 5, k_1 = 1$ , and  $k_2 = 2$ .

**2) Power Losses in Inductors:** The losses of the inductor can be separated into core loss ( $P_{\text{core}}$ ) and copper loss ( $P_{\text{copper}}$ ). The core loss includes the hysteresis loss, the eddy current loss, and the residual loss in the magnetic material. The copper loss includes the loss produced by the current at fundamental frequency and ripple current at the switching frequency in the windings. The power loss of the inductor differs with the type of winding, type of the core material, and the switching frequency.

**2-1) Copper Losses Calculation:** In general, the proximity and skin effects have contribution in the copper loss of the windings. In the case of the grid-side inductor  $L_{32}$ , the high-frequency ripple current is adequately mitigated by the filter to meet the requirements; thus, the power loss will only be as a result of the fundamental frequency current. The copper loss of the series inductors excluding inverter-side inductors can be calculated as

$$P_{\text{copper}} = I_{\text{RMS}}^2 R_{\text{dc}} + I_{\text{ac}}^2 R_{\text{ac}} \quad (26)$$

where  $I_{\text{RMS}}$  is the RMS value of the current in fundamental frequency and  $I_{\text{ac}}$  is the RMS value of the ac-ripple current

TABLE II  
PARAMETERS WHICH ARE USED FOR THEORETICAL CONVERTER LOSS CALCULATION

Parameter	Description	Typical Value
$I_{\text{RMS}1} LLCL$	RMS value of the current	5.8333 A
$I_{\text{RMS}1} L(LCL)_2$	RMS value of the current	5.8336 A
$R_F$	Equivalent ON-state resistance	0.1 $\Omega$
$C_{\text{oss}}$	Output capacitance	120 pF
$E_{\text{on}} + E_{\text{off}}$	Switching volt-ampere crossover energy losses	0.5 mJ

component. In (26),  $R_{\text{dc}}$  and  $R_{\text{ac}}$  are dc-resistance and the ac-resistance of the series inductances except the inverter side inductance. For the solid conductor copper with the American wire gauge of 22, the maximum frequency for 100% skin depth is 42 kHz. Consequently, it can be assumed that  $R_{\text{ac}} = R_{\text{dc}}$  in this study. The inverter-side inductor conduction loss is given by

$$P_{\text{LGS}} = I_{\text{RMS}1}^2 R_{\text{dc}1} \quad (27)$$

where  $R_{\text{dc}1}$  is the resistance of the inverter-side inductor and  $I_{\text{RMS}1}$  is the RMS inverter-side inductor current, given by

$$I_{\text{RMS}1}^2 = I_{\text{RMS}}^2 + \frac{\Delta i_{\text{pp}}^2}{12}. \quad (28)$$

**2-2) Core Loss Calculation:** The core loss can be found with the satisfactory accuracy using the Steinmetz equations supplied by the manufacturer's datasheet, using the following equation:

$$P_{\text{core}} = k(f^\alpha B^\beta V_e) \quad (29)$$

where  $k$ ,  $\alpha$ , and  $\beta$  are parameters of the material typically indicated by curve fitting;  $B$  is the flux density, in Tesla, and  $V_e$  is the magnetic core volume, in  $\text{cm}^3$ . The equation only works with a sinusoidal frequency and does not consider factors such as dc-offset.

## B. Inverter Loss Analysis

The power loss of the inverter can be calculated by evaluating the switching and the conduction losses of the power switches. The loss of each power switch can be written as follows [28]:

$$P_{Sx} = P_{\text{Scon}} + P_{\text{Ssw}} = [R_F I_{\text{RMS}1}^2] + [(E_{\text{on}} + E_{\text{off}}) + \frac{1}{2} C_{\text{oss}} V_{\text{in}}^2] f_s \quad (30)$$

where  $P_{\text{Scon}}$  and  $P_{\text{Ssw}}$  are the conduction and switching losses of the switch  $S_x$ , respectively,  $R_F$  is the equivalent resistance of the switch during ON state,  $E_{\text{on}}$  and  $E_{\text{off}}$  are volt-ampere crossover energy losses during the switch turn-ON and turn-OFF transitions, respectively,  $C_{\text{oss}}$  is the output capacitance of the switch, and  $V_{\text{in}}$  is the input voltage. Typical values which are used in the inverter, are presented in Table II. Using (30) and Table II, the efficiency of the inverter connected to a conventional  $LLCL$  filter is 95.2359% and the efficiency of the inverter connected to the proposed  $L(LCL)_2$  is 95.2357%. Therefore, it can be concluded that the increased current ripple which is due to the use of the  $L(LCL)_2$  filter, has a negligible effect on the efficiency of the inverter.

TABLE III  
POWER LOSSES OF THE  $L(LCL)_2$  FILTER AND THE  $LLCL$  FILTER

	$LLCL$ Filter	$L(LCL)_2$ Filter
$P_d$	0.0064 W	0.0345 W
$P_{copper}$	1.1840 W	1.1092 W
$P_{LGS}$	2.2865 W	1.6494 W
$P_{core}$	1.8238 W	1.3015 W
$P_{Sx}$	33.3487 W	33.3501 W
Total Loss	38.6494 W	37.4447 W

The power loss values of the  $L(LCL)_2$  filter and the  $LLCL$  filter are presented in Table III. It can be seen that besides high-frequency damping loss, other losses are less in the  $L(LCL)_2$  filter. However, the total power loss is decreased by 3.12%, compared to that of the  $LLCL$  filter.

## VI. CONCLUSION

In this paper, the principles of the conventional  $LLCL$  filter and parameter design of the  $L(LCL)_2$  filters were proposed. Since grid-side inductance ( $L_{21}$ ) of the  $LLCL$  filter is mainly decided by the harmonic currents around double the switching frequency instead of those around the switching frequency, it was replaced by a small trap at double the switching frequency. Compared to the  $LLCL$  filter, the replacement results in the reduction of the total inductance size, and hence, the total loss of the filter. The inverter-side inductance is divided into three parts to place resonant branches in between them. Therefore, the  $L(LCL)_2$  filter has lower loss and better performance at high-order harmonics attenuation. In the proposed design, the maximum power factor variation remained unchanged and the current THD improved by 7.77%.

A 700 W single-phase grid-tied inverter was designed to compare the characteristics of the conventional  $LLCL$  filter and the suggested  $L(LCL)_2$  filter through experimental results. In addition, the stability of the closed-loop system was analyzed. The results validate that the total loss and the value of the inductors of the  $L(LCL)_2$  filter reduced by a factor of 3.12% and 22.22%, respectively, compared to that of the  $LLCL$  filter.

## REFERENCES

- [1] A. Khalilnejad, A. Abbaspour, and A. Sarwat, "Multi-level optimization approach for directly coupled photovoltaic-electrolyser system," *Int. J. Hydrogen Energy*, vol. 41, no. 28, pp. 11884–11894, 2016. [Online]. Available: <http://www.sciencedirect.com/science/article/pii/S0360319915313938>
- [2] A. Anzalchi and A. Sarwat, "Artificial neural network based duty cycle estimation for maximum power point tracking in photovoltaic systems," in *Proc. IEEE SoutheastCon*, Apr. 2015, pp. 1–5, doi:10.1109/SECON.2015.7132988.
- [3] X. Fu, S. Li, and I. Jaithwa, "Implement optimal vector control for LCL-filter-based grid-connected converters by using recurrent neural networks," *IEEE Trans. Ind. Electron.*, vol. 62, no. 7, pp. 4443–4454, Jul. 2015, doi:10.1109/TIE.2015.2390140.
- [4] M. Liserre, F. Blaabjerg, and S. Hansen, "Design and control of an lcl-filter-based three-phase active rectifier," *IEEE Trans. Ind. Appl.*, vol. 41, no. 5, pp. 1281–1291, Sep. 2005, doi:10.1109/TIA.2005.853373.
- [5] D. Yang, X. Ruan, and H. Wu, "A real-time computation method with dual sampling mode to improve the current control performance of the LCL-type grid-connected inverter," *IEEE Trans. Ind. Electron.*, vol. 62, no. 7, pp. 4563–4572, Jul. 2015, doi:10.1109/TIE.2014.2327575.
- [6] X. Zhang, Y. Wang, C. Yu, L. Guo, and R. Cao, "Hysteresis model predictive control for high-power grid-connected inverters with output LCL filter," *IEEE Trans. Ind. Electron.*, vol. 63, no. 1, pp. 246–256, Jan. 2016, doi:10.1109/TIE.2015.2477060.
- [7] Y. Jiao, S. Lu, and F. C. Lee, "Switching performance optimization of a high power high frequency three-level active neutral point clamped phase leg," *IEEE Trans. Power Electron.*, vol. 29, no. 7, pp. 3255–3266, Jul. 2014, doi:10.1109/TPEL.2013.2277657.
- [8] W. Wu, P. Geng, X. Wang, Y. Ye, and T. Tang, "A novel control method for dual mode time-sharing cascaded sinusoidal inverter," in *Proc. IEEE 34th Annu. Conf.*, Nov. 2008, pp. 479–483, doi:10.1109/IECON.2008.4758000.
- [9] N. A. Ahmed, H. W. Lee, and M. Nakaoka, "Dual-mode time-sharing sinewave-modulation soft switching boost full-bridge one-stage power conditioner without electrolytic capacitor dc link," *IEEE Trans. Ind. Appl.*, vol. 43, no. 3, pp. 805–813, May 2007, doi:10.1109/TIA.2007.895803.
- [10] S. Saridakis, E. Koutroulis, and F. Blaabjerg, "Optimization of sic-based h5 and conergy-NPC transformerless pv inverters," in *Proc. IEEE Energy Convers. Congr. Expo.*, Sep. 2013, pp. 4732–4739, doi:10.1109/ECCE.2013.6647336.
- [11] P. Channegowda and V. John, "Filter optimization for grid interactive voltage source inverters," *IEEE Trans. Ind. Electron.*, vol. 57, no. 12, pp. 4106–4114, Dec. 2010, doi:10.1109/TIE.2010.2042421.
- [12] W. Wu, Y. He, and F. Blaabjerg, "An  $LLCL$  power filter for single-phase grid-tied inverter," *IEEE Trans. Power Electron.*, vol. 27, no. 2, pp. 782–789, Feb. 2012, doi:10.1109/TPEL.2011.2161337.
- [13] J. M. Bloemink and T. C. Green, "Reducing passive filter sizes with tuned traps for distribution level power electronics," in *Proc. IEEE Conf. Power Electron. Appl.*, Aug. 2011, pp. 1–9.
- [14] J. Huang and H. Shi, "A hybrid filter for the suppression of common-mode voltage and differential-mode harmonics in three-phase inverters with cpm," *IEEE Trans. Ind. Electron.*, vol. 62, no. 7, pp. 3991–4000, Jul. 2015, doi:10.1109/TIE.2014.2381162.
- [15] Y. Liu, W. Wu, Y. He, Z. Lin, F. Blaabjerg, and H. S. H. Chung, "An efficient and robust hybrid damper for LCL- or LLCL-based grid-tied inverter with strong grid-side harmonic voltage effect rejection," *IEEE Trans. Ind. Electron.*, vol. 63, no. 2, pp. 926–936, Feb. 2016, doi:10.1109/TIE.2015.2478738.
- [16] J. Ji, W. Wu, Y. He, Z. Lin, F. Blaabjerg, and H. S. H. Chung, "A simple differential mode emi suppressor for the lcl-filter-based single-phase grid-tied transformerless inverter," *IEEE Trans. Ind. Electron.*, vol. 62, no. 7, pp. 4141–4147, Jul. 2015, doi:10.1109/TIE.2014.2385666.
- [17] D. Pan, X. Ruan, C. Bao, W. Li, and X. Wang, "Optimized controller design for lcl-type grid-connected inverter to achieve high robustness against grid-impedance variation," *IEEE Trans. Ind. Electron.*, vol. 62, no. 3, pp. 1537–1547, Mar. 2015, doi:10.1109/TIE.2014.2341584.
- [18] *IEEE Recommended Practice and Requirements for Harmonic Control in Electric Power Systems*, IEEE Std 519-2014 (Revision of IEEE Std 519-1992), Jun. 2014, pp. 1–29, doi:10.1109/IEEESTD.2014.6826459.
- [19] *IEEE Application Guide for IEEE Std 1547(tm), IEEE Standard for Interconnecting Distributed Resources With Electric Power Systems*, IEEE Std 1547.2-2008, Apr. 2009, pp. 1–217, doi:10.1109/IEEESTD.2008.4816078.
- [20] B. Bolsens, K. D. Brabandere, J. V. den Keybus, J. Driesen, and R. Belmans, "Model-based generation of low distortion currents in grid-coupled pwm-inverters using an lcl output filter," *IEEE Trans. Power Electron.*, vol. 21, no. 4, pp. 1032–1040, Jul. 2006, doi:10.1109/TPEL.2006.876840.
- [21] G. r. Zhu, H. Wang, B. Liang, S. C. Tan, and J. Jiang, "Enhanced single-phase full-bridge inverter with minimal low-frequency current ripple," *IEEE Trans. Ind. Electron.*, vol. 63, no. 2, pp. 937–943, Feb. 2016, doi:10.1109/TIE.2015.2491881.
- [22] G. Grandi, J. Loncarski, and O. Dordevic, "Analysis and comparison of peak-to-peak current ripple in two-level and multilevel pwm inverters," *IEEE Trans. Ind. Electron.*, vol. 62, no. 5, pp. 2721–2730, May 2015, doi:10.1109/TIE.2014.2363624.
- [23] K. Jalili and S. Bernet, "Design of lcl filters of active-front-end two-level voltage-source converters," *IEEE Trans. Ind. Electron.*, vol. 56, no. 5, pp. 1674–1689, May 2009, doi:10.1109/TIE.2008.2011251.
- [24] X. Zheng, L. Xiao, Y. Lei, and Z. Wang, "Optimisation of LCL filter based on closed-loop total harmonic distortion calculation model of the grid-connected inverter," *IET Power Electron.*, vol. 8, no. 6, pp. 860–868, 2015, doi:10.1049/iet-pel.2014.0651.

- [25] A. Singh, A. K. Kaviani, and B. Mirafzal, "On dynamic models and stability analysis of three-phase phasor pwm-based csi for stand-alone applications," *IEEE Trans. Ind. Electron.*, vol. 62, no. 5, pp. 2698–2707, May 2015, doi:10.1109/TIE.2014.2363814.
- [26] C. A. Busada, S. G. Jorge, and J. A. Solsona, "Full-state feedback equivalent controller for active damping in lcl-filtered grid-connected inverters using a reduced number of sensors," *IEEE Trans. Ind. Electron.*, vol. 62, no. 10, pp. 5993–6002, Oct. 2015, doi:10.1109/TIE.2015.2424391.
- [27] W. Wu, Y. He, T. Tang, and F. Blaabjerg, "A new design method for the passive damped LCL and LLCL filter-based single-phase grid-tied inverter," *IEEE Trans. Ind. Electron.*, vol. 60, no. 10, pp. 4339–4350, Oct. 2013, doi:10.1109/TIE.2012.2217725.
- [28] M. Moghaddami, A. Anzalchi, and A. Sarwat, "Single-stage three-phase ac-ac matrix converter for inductive power transfer systems," *IEEE Trans. Ind. Electron.*, to be published, doi:10.1109/TIE.2016.2563408.



**Arash Anzalchi** (S'14) received the B.S. and M.S. degrees in electrical engineering from K.N. Toosi University of Technology and Science and Research Branch, Islamic Azad University, Tehran, Iran, in 2007 and 2011, respectively. He is currently working toward the Ph.D. degree in electrical engineering at Florida International University, Miami, FL, USA.

He is currently a Graduate Assistant at Florida International University. He is also one of the researchers of the "Energy Power Reliability and

Analytic Center (EPRAC)," which conducts high-end studies on the effect of high-penetration PV integration into the distribution grid. His research interests include photovoltaic integration into the distribution grid, mitigation of power quality issues, and smart power electronic technologies for renewable energy sources.



**Masood Moghaddami** (S'15) received the B.S. degree from Amirkabir University of Technology, Tehran, Iran, in 2009, and the M.S. degree from Iran University of Science and Technology, Tehran, in 2012, both in electrical engineering. He is currently working toward the Ph.D. degree in the Department of Electrical and Computer Engineering, Florida International University, Miami, FL, USA.

From 2011 to 2014, he worked in industry as an Engineer designing optimization of large power transformers. His research interests include finite-element analysis, power electronics, contactless power transfer, and renewable energy systems.



**Amir Moghaddasi** (S'11) received the B.Sc. degree from Shaded University, Tehran, Iran, in 2007, the M.Sc. degree from Iran University of Science and Technology (IUST), Tehran, in 2009, and the Ph.D. degree from Florida International University, Miami, FL, USA, in 2016, all in electrical engineering.

He is currently a Research Scholar at Florida International University. His research interests include high-penetration renewable systems, power quality issues in microgrids, design and control of power converters, and application of computational intelligence techniques in power systems.



**Arif I. Sarwat** (M'08–SM'16) received the M.S. degree in electrical and computer engineering from the University of Florida, Gainesville, FL, USA, in 2005, and the Ph.D. degree in electrical engineering from the University of South Florida, Tampa, FL, in 2010.

He worked in industry (SIEMENS) for nine years, executing many critical projects. Before joining Florida International University, Miami, FL, USA, as an Assistant Professor, he was an Assistant Professor of electrical engineering at

the University at Buffalo, State University of New York, Buffalo, NY, USA. His significant work in energy storage, microgrid, and DSM is demonstrated by Sustainable Electric Energy Delivery Systems in Florida. His research interests include smart grids, high-penetration renewable systems, power system reliability, large-scale distributed generation integration, large-scale data analysis, cyber security, and vehicular technology.



**Akshay Kumar Rathore** (M'05–SM'12) received the M.Tech. degree in electrical machines and drives from the Indian Institute of Technology (BHU), Varanasi, India, in 2003, and the Ph.D. degree in power electronics from the University of Victoria, Victoria, BC, Canada, in 2008.

He had two subsequent postdoctoral research appointments with the University of Wuppertal, Germany, and the University of Illinois at Chicago, Chicago, IL, USA. From November 2010 to February 2016, he was an Assistant Professor in the Department of Electrical and Computer Engineering, National University of Singapore, Singapore. He is currently an Associate Professor in the Department of Electrical and Computer Engineering, Concordia University, Montreal, QC, Canada. He has published more than 140 research papers in international journals and conference proceedings including 48 IEEE TRANSACTIONS. He is a Lead Researcher in current-fed converters.

Dr. Rathore is an Associate Editor of the IEEE TRANSACTIONS ON INDUSTRIAL APPLICATIONS, IEEE TRANSACTIONS ON INDUSTRIAL ELECTRONICS, IEEE TRANSACTIONS ON TRANSPORTATION ELECTRIFICATION, IEEE TRANSACTIONS ON SUSTAINABLE ENERGY, and IEEE JOURNAL OF EMERGING AND SELECTED TOPICS IN POWER ELECTRONICS. He received the Gold Medal during his M.Tech. studies for securing the highest academic standing among all electrical engineering specializations. He also received the University Ph.D. Fellowship, Thouvenelle Graduate Scholarship, the 2013 IEEE IAS Andrew W. Smith Outstanding Young Member Award, and the 2014 Isao Takahashi Power Electronics Award.